COUPLED MACRO-MICRO MODELLING OF THE SECONDARY MELTING OF TURBINE DISC SUPERALLOYS

P.D. Lee, R. Lothian, L.J. Hobbs, and M. McLean Department of Materials, Imperial College London, UK

Abstract

A model of the macroscopic fluid flow, heat transfer and electromagnetic effects during secondary melting was developed and coupled to microstructural feature prediction. The importance of the different driving forces on the macroscopic model was explored using the test cases of vacuum arc remelting (VAR) and electron beam button melting (EBBM) of IN718. The predictions of the surface flows and final microstructure in the EBBM process were compared to experimental results.

Introduction

The demands of the aerospace industry have led to the development of a range of alloys with specific properties to satisfy the design requirements for different parts of the gas turbine engine. For turbine blades, the need is for a balance of very high temperature (up to ~1100°C) creep strength and corrosion resistance, whilst turbine discs have lower operating temperatures (~800°C). However, the demands for increasing power, through higher turbine speeds with associated increased centrifugal forces, and reduced engine weight have required significant increases in stresses carried by the discs. The development of alloys for turbine disc applications has concentrated on increasing the yield strength of the materials bringing a concomitant decrease in toughness, which has made the fracture characteristics of these materials very sensitive to the presence of defects. Consequently, it is now standard practice to improve the quality of turbine disc alloys, initially produced by vacuum induction melting (VIM), by subjecting them to one or more secondary melting processes. These processes include vacuum arc re-melting (VAR), electroslag re-melting (ESR) and electron beam cold hearth refining (EBCHR). The quality improvements obtained are a finer microstructure, less macrosegregation and a reduced inclusion content.

In the past, the design and optimisation of secondary melting processes for new alloys has involved a great deal of expensive trial and error. Numerical modelling can, in principle, provide a less expensive route to reliable and efficient alloy processing. This paper evaluates the viability of combining macroscopic process models with empirical and theoretical treatments of microstructure formation for the accurate prediction of the ingot microstructure and defect susceptibility.

Theory

Macro-Model

There are many factors involved in the VAR process. Correspondingly, a detailed description of the real installation being modelled and accurate thermophysical data for the alloy involved must be supplied to any model which aspires to give accurate predictions. Factors to be dealt with include: heat transfer, fluid flow, magnetohydrodynamics (including both the Lorentz force and Joule heating), and solidification.

The modelling of the heat transfer, fluid flow, and solidification was performed using the commercial finite volume code Fluent with subroutines added to handle the spatially and temporally varying heat flux and surface tension gradient boundary conditions. The calculation of the Lorentz force and Joule heating was also coded in, but proved an insignificant effect in EBBM, although it is crucial in VAR. The equations being solved are listed below.

Energy Equation

The energy equation to be solved is:

$$\frac{\partial}{\partial t}(\rho h) + \nabla \cdot (\rho \mathbf{u} h - k \nabla T - \tau \cdot \mathbf{u}) = \frac{\partial p}{\partial t} + \mathbf{u} \cdot \nabla p + S_h, \tag{1}$$

where h is the static enthalpy, p is the static fluid pressure, ρ is the density, k is the thermal conductivity, t is time, \mathbf{u} is the fluid velocity, T is temperature and τ is the viscous stress tensor. S_h represents heat sources, including Joule heating (VAR), electron beam heating (EBBM), energy losses by radiation and conduction and latent heat evolution. The last of course, plays a crucial role in solidification modelling.

Momentum and Continuity Equations

The velocity of liquid, \mathbf{u} , is given by the momentum equation¹:

$$\frac{\partial}{\partial t}(\rho \mathbf{u}) + \nabla \cdot (\rho \mathbf{u} \otimes \mathbf{u} + p\mathbf{I} - \tau) = \rho \mathbf{g} + \mathbf{F}, \tag{2}$$

where I is the 3x3 identity tensor, g is the gravitational acceleration, and F is the sum of all other body forces (e.g. the Marangoni force or the Lorentz force).

The stress tensor τ has components:

$$\tau_{ij} = \left[\mu \left(\frac{\partial u_i}{\partial x_j} + \frac{\partial u_i}{\partial x_i}\right)\right] - \frac{2}{3}\mu \frac{\partial u_l}{\partial x_l} \delta_{ij} , \qquad (3)$$

where u is the viscosity.

To solve for the momentum and pressure, the mass conservation equation must also be satisfied:

$$\frac{\partial \rho}{\partial t} + \nabla \cdot (\rho \mathbf{u}) = S_m. \tag{4}$$

 S_m is the mass added to the continuous phase from any dispersed phase or as a source (e.g. due to droplets from the consumable electrode). In the present work, S_m has been taken to be zero, since filling is not modelled.

Electromagnetic Effects

The magnetic induction ${\bf B}$ in a magnetised fluid is calculated from the induction equation:

$$\frac{\partial \mathbf{B}}{\partial t} = \nabla \times (\mathbf{u} \times \mathbf{B}) + \eta \nabla^2 \mathbf{B} . \tag{5}$$

Here $\eta = (\mu_e \sigma)^{-1}$ is the magnetic diffusivity, where μ_e is the magnetic permeability (assumed in this work to take its vacuum value μ_0) and σ is the conductivity of the fluid. In the steady state, the LHS of (5) is zero. Furthermore, we may estimate the relative magnitudes of the terms on the RHS. The ratio of the first term, representing advection of field by the flow, to the second, representing field diffusion through Joule dissipation is given by the magnetic Reynolds number:

$$R_{\rm m} = \frac{L v}{\eta} \,. \tag{6}$$

The length scale L is typically 1 m in industrial scale remelting processes and $\eta \approx 1~\text{m}^2/\text{s}$, so the diffusion term dominates if the typical flow velocity v is much less than 1m/s. R_m is correspondingly smaller on the smaller scales of pilot VAR and EBBM melts. It has been normal to neglect the advection term in such studies and this approach is justified a posteriori if computed velocities are indeed small. With these assumptions, **B** decouples from the fluid flow and may be calculated from the equation:

$$\nabla^2 \mathbf{B} = 0. \tag{7}$$

This equation was solved subject to the imposition of normal current components on the boundaries of the ingot.

The current density, J, Lorentz Force, F_e , and Joule heating, Q_{joule} , were calculated from the equations:

$$\mu_0 \mathbf{J} = \nabla \mathbf{x} \mathbf{B}, \tag{8}$$

$$\mathbf{F}_{\mathbf{e}} = \mathbf{J} \times \mathbf{B} \tag{9}$$

and

$$Q_{\text{joule}} = \frac{\mathbf{J} \cdot \mathbf{J}}{\sigma}.$$
 (10)

In practice, a 2-D axisymmetric model, which considerably reduces computing time, was adopted.

Micro-Models

As summarised by McLean² the primary dendrite arm spacing, λ_1 , in superalloys has been shown by many authors to be a function of the thermal gradient and the growth velocity both experimentally and theoretically. Recently Lu and Hunt³ developed a numerical model of cellular and dendritic growth to predict the cell and dendrite spacing as well as the undercooling at the tip. Hunt and Lu⁴ provided an analytic expression fitted to their numerical model results that predicts the minimum stable half-spacing of dendrites.

Cast in terms of non-dimensional parameters*, Hunt and Lu found for the case of $G' > 1 \times 10^{-10}$ and 0.068 < k < 0.69 that the dimensionless dendrite half spacing, λ' , is given by:

$$\lambda' = 0.7798 \times 10^{-1} V^{(a-0.75)} (V' - G')^{0.75} G^{-0.6028},$$
 (11)

where:

$$a = -1.131 - 0.1555\log_{10}(G') - 0.7589 \times 10^{-2} [\log_{10}(G')]^{2}.$$
 (12)

To determine λ_1 the thermal gradient and front velocity were calculated using the macro-model. As a cell passes through the liquidus temperature the nearest neighbours' temperatures were used to calculate the thermal gradient normal to the isotherm. Hunt and Lu specify G as the solid thermal gradient, referring to the dendrite tip as the solid. In the macro model the mushy zone is treated as a continuum, making the thermal gradient close to the liquidus temperature an appropriate approximation for G.

The value of V used to determine λ_1 was the velocity of the liquidus isotherm, V_{liq} . This velocity was determined using a central difference approximation of the following derivative:

$$V_{liq} = \frac{\partial n}{\partial t} \Big|_{T = T_{liq}} = \frac{1}{\frac{\partial t}{\partial n} \Big|_{T = T_{liq}}} = \frac{1}{\frac{\partial t_l}{\partial n}},$$
 (13)

where t_i is the time at which the local temperature attains the liquidus value and n is the direction normal to the liquidus isotherm.

The ripening or local solidification time t_s , is defined as the time for which the dendrite is in the mushy zone. The secondary dendrite arm spacing, λ_2 , is related to t_s by:

$$\lambda_2 = -7.0 + 12.5 t_s^{0.33} [\mu m].$$
 (14)

The carbide size, λ_{carb} , has also been shown experimentally to be a function of the local solidification time by Jardy *et al.*⁵, who suggests the following formula for IN718:

$$\lambda_{carb} = \sqrt[3]{80.9 + 9.16t_s} \ [\mu \text{m}]. \tag{15}$$

Comparison of Different Driving Forces

In order to estimate the relative importance of Lorentz, Marangoni and buoyancy forces, the relevant dimensionless numbers are constructed using the typical magnitudes listed in Table I.

To compare the relative importance of Marangoni and buoyancy forces, we evaluate the dimensionless quantity:

$$M = \frac{\frac{\partial \gamma}{\partial T}}{\frac{\partial \rho}{\partial T} L^2 g}.$$
 (16)

^{*} The non-dimensional parameters are $G' = \frac{G\Gamma k}{\Delta T_o^2}$, $V' = \frac{V\Gamma k}{D\Delta T_o}$ and $\lambda' = \frac{\lambda \Delta T_o}{\Gamma k}$,

where ΔT_o is the undercooling for a planar front given by $\Delta T_o = \frac{mC_o(k-1)}{k}$. G, V,

 $[\]Gamma$, D, m, C_o , and k are respectively the solid temperature gradient, velocity, Gibbs-Thomson coefficient, liquid diffusion coefficient, liquidus slope, bulk composition, and distribution coefficient⁴.

Table I. Nominal properties used to calculate the relative importance of the driving forces during EBBM and VAR of nickel based superalloys.

Property	Symbol	EBBM	VAR	Units
Density	ρ	8000	8000	kg/m³
Characteristic length	L	0.01	0.1	m
Surface tension gradient	∂γ/∂ <i>T</i>	-1×10^{-4}	$-1x10^{-4}$	N/m/K
Density gradient	$\partial \rho / \partial T$	0.1	0.1	kg/m³/K
Beam/arc current	I	0.35	5000	Α
Beam/arc radius	a	0.005	0.1	m
Pool superheat	ΔT	200	200	K

In EBBM, M≈1, indicating that these forces are of comparable magnitude. In VAR, since M≈0.01, buoyancy forces are much greater than Marangoni forces.

We now estimate the typical value of the Lorentz force in the two processes. Assuming the current is spread evenly over a disc of radius a, we find that the average force is given by:

$$F_{e} = \frac{\mu_{0} I^{2}}{3\pi^{2} a^{3}}$$
 (17)

We compare this with the typical buoyancy force:

$$F_{b} = \frac{\partial \rho}{\partial T} \Delta T \mathbf{g} \tag{18}$$

and find that $\frac{F_c}{F_b} \approx 2 \times 10^{-4}$ in EBBM, demonstrating that only buoyancy and Marangoni forces are important in determining the fluid flow. Conversely, in VAR, $\frac{F_c}{F_b} \approx 5$ and electromagnetic forces are comparable to buoyancy throughout the melt pool. Note that magnetic forces are dependent on the square of the current in the melt, so loss of half of the current would reduce these forces by a factor of four. Hence, it is important to know what proportion of the current reaches the ingot in a real installation. Evaluation of the Joule heating indicates that it is not significant in either process.

VAR Model

Validation

To validate the macromodel it was compared to previously published work simulating the VAR process (shown schematically in Figure 1). The model was run with the values given by Jardy and Ablitzer⁶ in their study of fluid flow during the pilot scale VAR remelting of Zy4. They measured the pool shape experimentally (drawn as the dashed line in Figure 2) and used it as a boundary condition to determine the flow by solving the Navier-Stokes, Maxwell's, and Fourier equations. They assumed steady state and treated the problem as axisymmetric. With these conditions they calculated a maximum velocity of 0.013 m/s when half of the melting current reaches the pool, or $\alpha = 0.5$. In this study the location of the solidification front was not pre-specified, as it was by Jardy and Ablitzer, therefore values of the heat transfer coefficient, h_c , and the latent heat had to be approximated and are listed in Table II. A grid of 30x100 control volumes was used to simulate the 0.1x0.5 m domain.

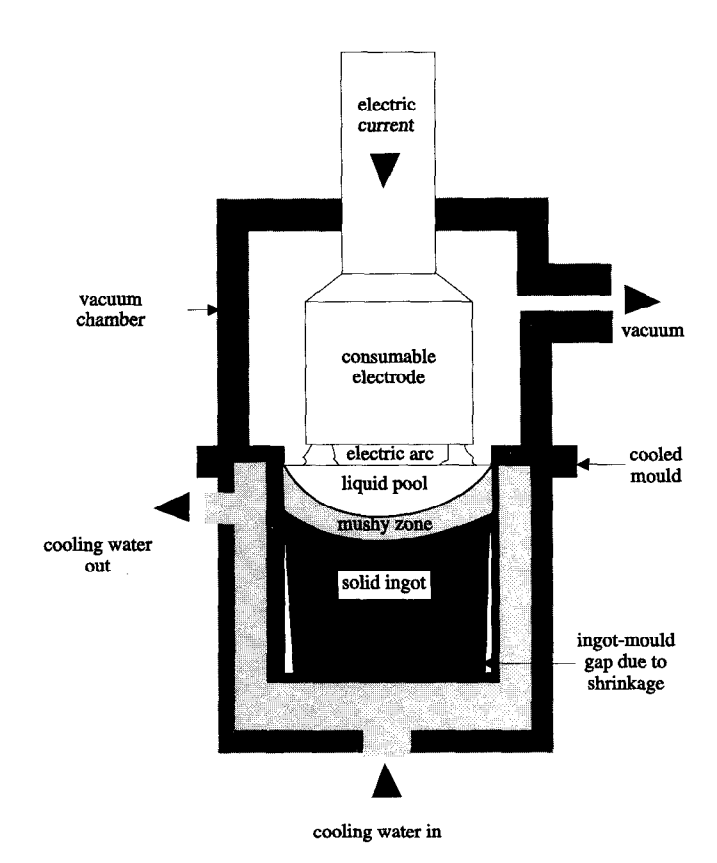


Figure 1. Schematic diagram of a VAR installation.

Table II. Approximated values used for VAR comparison simulation to Jardy and Ablitzer⁶ and for calculating typical microstructural features.

Property		Value	Units
Density		6000-0.1 <i>T</i>	kg/m ³
Ingot radius		0.10	m
Electrode (arc) radius	r	0.08	m
Arc current		5000 x α	Α
Liquidus temperature	T_l	2073	K
Solidus temperature	T_s	2023	K
Latent heat	L	200,000	J/kg
h_c for top 0.05 m of	h_c	3000, (T _{amb} =273 K)	W/m^2
ingot/crucible contact			2
h_c for rest of ingot/crucible	h_c	100, $(T_{amb}=273 \text{ K})$	W/m^2
contact			
Emissivity	ε	0.2 , $(T_{amb}=273 \text{ K})$	
Gibbs-Thomson coefficient	Г	2×10^{-7}	mK
Liquid diffusion coefficient	D	5 x 10 ⁻⁹	m^2/s
liquidus slope	m	-4	K/wt.%
bulk composition	Co	20	wt.%
distribution coefficient	k	0.2	

The flow patterns and molten pool shapes predicted in the present study are shown in Figures 2(a) to 2(c) for α values of 0, 0.5, and 1 respectively. The maximum velocity predicted with $\alpha = 0.5$ is 0.015 m/s, in excellent agreement with Jardy and Ablitzer's value of 0.013 m/s, with the difference possibly due to the pool shape being calculated rather than imposed.

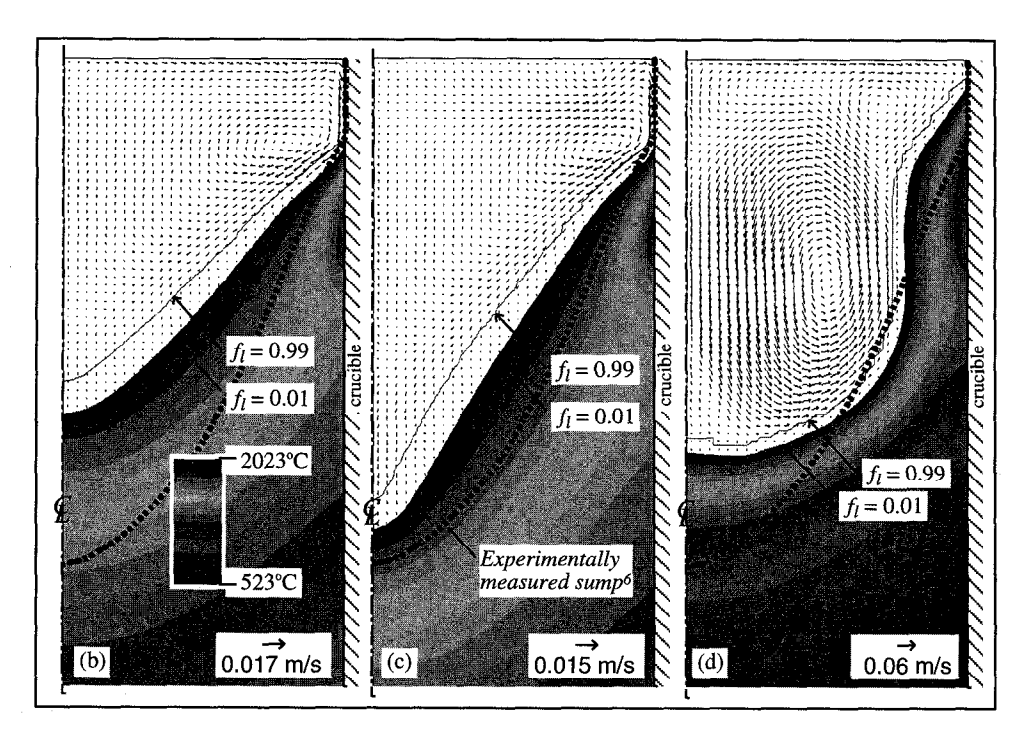


Figure 2. Calculated pool shape and velocity fields in a VAR ingot for: (a) α =0.0; (b) α =0.5; and (c) α =1.0. The pool shape measured by Jardy and Ablitzer⁶ is shown as the heavy dashed line.

Comparing the pool shapes calculated in the present study to that experimentally measured by Jardy and Ablitzer, the experimentally measured pool shape appears to fall between the $\alpha = 0.5$ and $\alpha = 1.0$ predictions (see Figures 2(b) and 2(c)). The calculated pool shape is strongly dependent on the heat transfer coefficient which was not known, hence the difference in pool depth can be attributed to any error in the approximate values used for h_c .

Microstructural Predictions

The importance of the melt pool shape on the final properties is illustrated by comparing the microstructural predictions for the two extremes of VAR with no EMF calculation (Figure 2(a)) and with the full melting current transferred (Figure 2(c)). Using the macromodel to determine G and V and the approximate values for the material properties as listed in Table II, the values for λ_1 were calculated using equation (11) and are shown in Figure 3.

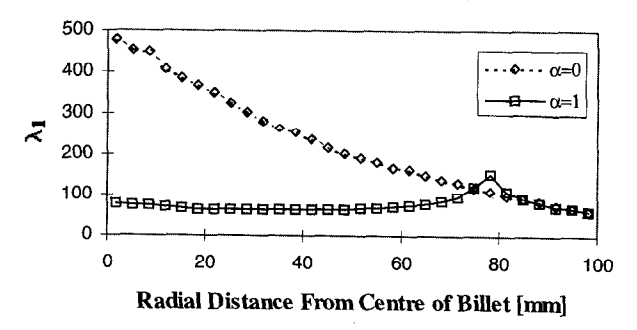


Figure 3. Predicted λ_1 values in a VAR ingot for α =0.0 and α =1.0.

When $\alpha=0$, the flow at the bottom of the sump is slow and the isotherms become stratified, with small thermal gradients, as is seen by the distance between the $f_i=0.01$ and $f_i=0.99$ contours. This leads to large λ_1 predictions. The strong counter-clockwise flow when $\alpha=1$ produces much higher gradients, and hence significantly smaller λ_1 predictions.

Using equation (14) the predictions for λ_2 are shown in Figure 4. Because the simulation was steady state, the value for t_s was calculated by taking the distance between T_s and T_l parallel to the pull direction and dividing by the pull velocity. This reaches an extreme condition when the solidification front is perpendicular to the pull direction, as is the case at a radius of 78 mm for the $\alpha=1.0$ simulation. The primary dendrites are growing normal to the pull velocity, giving a long ripening time for the secondary arms. For most of the ingot, the EMF increases the thermal gradients.

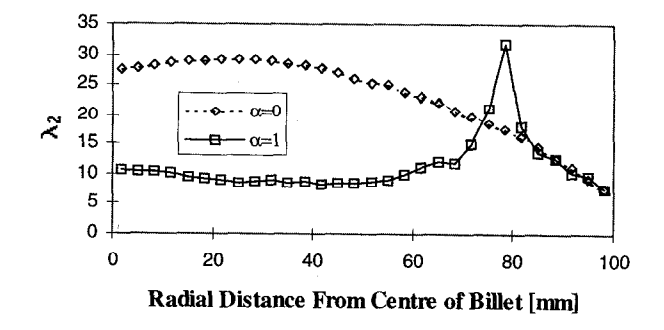


Figure 4. Predicted λ_2 values in a VAR ingot for α =0.0 and α =1.0.

reducing the size of the mushy zone, and hence producing a finer microstructure or smaller λ_2 values. However, the interaction of the EMF on the pool shape produces a region of growth normal to the pull direction, giving an inversion of the general trend. Comparing of the predicted λ_2 values for the two cases in Figure 4 illustrates the importance of including the EMF and of calculating the pool shape rather than specifying it *a priori* since both have strong influences on the final ingot microstructure.

Electron Beam Button Melting Model

Experimental Methods

The forming of a button by electron beam melting into a copper cooled hemispherical crucible of 168 mm diameter can be summarised by the following steps:

- i. crucible and electrode preheating;
- ii. electrode tip shaping
- iii. melting of the electrode with the molten metal dripping into the crucible and a fraction of the power being applied to the partially formed button.
- iv. controlled solidification of the fully formed button.

The model results were compared to two different types of experimental runs performed at the National Physical Laboratory, Teddington, UK. The first type was designed to allow characterisation of the surface flow velocities. The second type were the standard runs designed to give a controlled solidification pattern that concentrates inclusions into a central raft for simplified cleanliness characterisation. The two types of runs differ significantly only in the final stage, iv.

As described by Quested et al.⁷, the first type of run approximates a stationary beam at the centre of the button. However, since the electron beam, even though partially defocused, distributes power over a circle with a radius less than 20 mm, the beam was scanned circumferentially at a high frequency on the surface of the button. The centre of the beam circumscribes the centre of the button at a radius varying linearly from 0 to 20 mm three times over the period of 60 s. Al₂O₃ particles were added to the surface and the motion of these particles was tracked using a video camera to provide rough quantitative surface flow velocities.

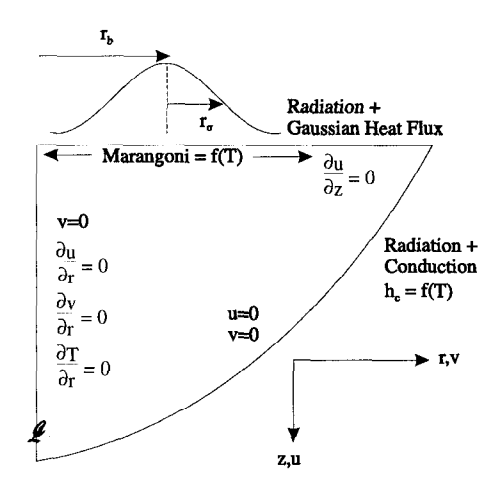


Figure 5. Schematic diagram showing the geometry and boundary conditions used to model the EBBM process.

The second type of run was a normal practice solidification cycle used to concentrate inclusions at the centre of the button, often forming a visible raft. Quested *et al.*⁷ suggested that the raft is caused by radial flow inward during stage iv, where the beam scans from the outer radius into the centre of the button. This inward radial motion is at a constant speed over a period ranging from 40 to 120 s. Simultaneously the current is decreased linearly from full power to 0 mA.

The buttons were examined metallographically after casting, to measure the microstructural features. The secondary dendrite arm spacing measurements, were obtained from longitudinal sections of the button which were polished and then etched in Marble's reagent (HCL 50 ml, saturated cupric sulphate solution 25 ml and distilled water 25 ml). Using an SEM, the length of five consecutive secondary arms was measured and averaged to determine the spacing. The primary dendrite arm spacing, measurement technique and results are given by Ellis⁸.

Problem Formulation

The heat transfer and fluid flow was modelled in EBBM assuming that the flow was axisymmetric as was the distribution of heat from the electron beam. The model was solved on a grid of 40x40 control volumes for transient flow using an implicit solution with 0.5 s time steps. A steady state solution was obtained to use as an initial condition assuming a highly defocussed beam centred half way out the radius. The geometry and boundary conditions used are shown in Figure 5. The material properties used are listed in Table III or given in Figure 6 as a function of temperature.

Table III. Values used to simulate EBBM processing of IN718. (Note that f(t) indicates the value is a function of time whilst f(T) indicates a function of temperature.)

Property	Symbol	Value	Units			
Button radius		37	mm			
Button depth		25	mm			
Beam current	I	f(t)	mA			
Beam voltage	V	25	kV			
Beam focal radius	r_{σ}	10	mm			
Beam location radius	r_b	f(<i>t</i>)	mm			
Density	ρ	f(<i>T</i>)	kg/m ³			
Specific heat capacity	Cp	f(<i>T</i>)	J/kg/K			
Viscosity	υ	$5x10^{-3}$	kg/m s			
Surface tension gradient:	$\partial \gamma / \partial T$	f(<i>T</i>)	N/m/K			
Liquidus temperature	T_l	1609	K			
Solidus temperature	T_s	1533	K			
Latent heat	L	270,000	J/kg			
Ingot/crucible h_c	h_c	$f(T_{ingot}),$	W/m^2			
		$(T_{amb} = 500 \text{ K})$				
Ingot/crucible emissivity	ε	0.3,				
		$(T_{amb} = 500 \text{ K})$				
Button top emissivity	ϵ_{top}	0.25,				
		$(T_{amb}=273 \text{ K})$				

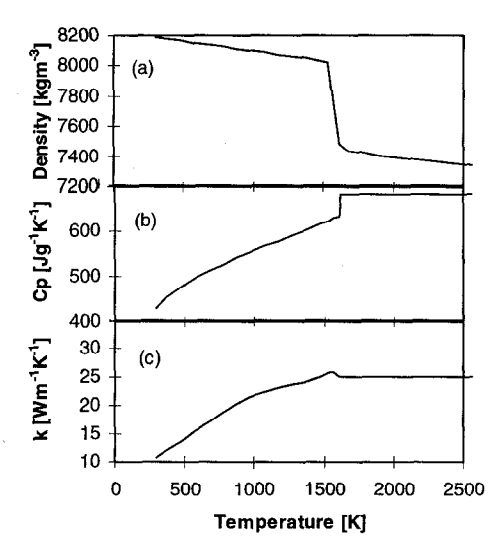


Figure 6. The temperature dependent material properties used in the EBBM simulations. (a) Density; (b) specific heat capacity; and (c) the thermal conductivity.

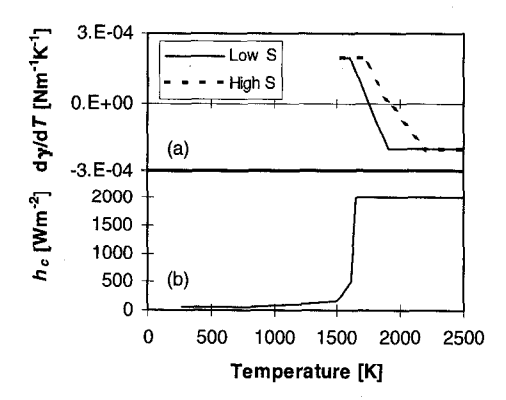


Figure 7. The temperature dependent values for (a) $\partial \gamma \partial T$ and (b) the heat transfer coefficient used in the EBBM simulations.

The values for $\partial \gamma \partial T$ were estimated using values provided by Mills⁹ and assuming the behaviour is similar to that of sulphur in Fe-Ni-Cr alloys as determined by McNallan and Debroy¹⁰. The values were included as a piece-wise linear fit. The values used are shown in Figure 7(a) for the two cases of low surfactant concentration (6 ppm S, <10 ppm O), and high surfactant concentration (20 ppm S, 8 ppm O), the CPQ and CPZ compositions of IN718 as given by Quested *et al.*⁷ respectively.

The values for the heat transfer coefficient between the ingot and mould wall, h_c , were calculated from measurements of the heat flux into a copper crucible made during the plasma remelting of IN718 into a 125 mm diameter cylindrical ingot. The heat flux was divided into radiative, convective, and contact components, with the h_c value representing the contact portion.

Starting with a steady state solution, the process was modelled with the transient boundary condition of the electron beam moving across the surface providing a Gaussian distribution of heat flux, Q, characterised by:

$$Q(R) = Q_o e^{-\frac{R^2}{r_\sigma^2}},$$
 (19)

where R is the distance from the beam centre, r_{σ} is the beam focal radius, and Q_o is the total flux. Given that the beam circumscribes the centre of the button at a radius of r_b , the averaged heat flux, $Q_{\theta}(r)$, can be obtained by integrating Q by $d\theta$, giving:

$$Q_{\theta}(r) = \frac{1}{\pi} \int_{0}^{\pi} Q(R) \, d\theta = Q_{\theta} e^{-\frac{r^{2} + r_{b}^{2}}{r_{\sigma}^{2}}} I_{0} \left(\frac{2rr_{b}}{r_{\sigma}^{2}}\right), \tag{20}$$

where I_0 is the modified Bessel function of the first kind and order 0.

Surface Flow Predictions

Using the model as outlined in the previous section, two experimental runs were simulated, both with the same boundary conditions but with the low and high sulphur content being represented by the variation in $\partial \gamma / \partial T$ as a function of T. The electron beam motion was the same for both cases:

- 30 seconds of r_b varying from 25 to 5 mm over 2 second cycles at a power of 6 kW;
- 30 seconds with no heat flux (during which time the Al₂O₃ particles were added);
- iii. and finally 60 seconds of r_b varying from 20 to 0 mm over 20 second cycles at a power of 6 kW.

For the case of low S the surface flow was outwards from the centre of the beam with the particles reaching a maximum velocity of approximately 0.06 m/s. The particles travelled near to the edge of the pool, but a small inward surface flow was present in the outermost region of the pool. The predicted flow pattern 78 seconds into the simulation (seconds after the pool surface had become fully molten) is shown in Figure 8(a). The predicted surface flow is outwards with a maximum value of 0.16 m/s. The predicted value is higher than the maximum velocities observed experimentally, however, the Al₂O₃ particles were not tracked in the high velocity region. As observed experimentally, a small recirculating inward flow near the edge is predicted, with a time dependent size and peak velocity. This flow is caused by the positive value of $\partial \gamma / \partial T$ at temperatures less than 1750 K, and the size of inward flow is a function of the location of this isotherm, which is in turn dependent on the stage of remelting and the value

For the high S experiments, the particles were observed to move inwards from the edge of the pool peak velocities of 0.19 m/s, moving at highest velocity shortly after leaving the edge of the pool, slowing to velocities of approximately 0.1 m/s half way towards the centre. The particles stop before reaching the centre but on the inside of r_b . Figure 8(b) shows the predicted flow pattern 78 seconds into the simulation. This period is when the velocities were recorded experimentally. The predicted surface flow pattern is identical to that observed experimentally, with the flow going from the outside into the centre, but turning down just before reaching the centre. The maximum velocity predicted is 0.14 m/s, lower than that observed experimentally (0.19 m/s). This suggests that the value for $\partial \gamma \partial T$ may be greater than that used in the simulation, or the inversion point to a negative value could be at a higher temperature.

Comparing the two cases, a reduction in the rate of change of $\partial \gamma / \partial T$ from a positive to negative value and a 150°C increase in the inversion point, dramatically changed the flow patterns and location of the liquidus front. The size of the mushy zone is also altered, and hence the microstructural features will be different. A comparison of Figure 8(a) to Figure 8(b) illustrates the dominance of Marangoni flow in the EBBM process.

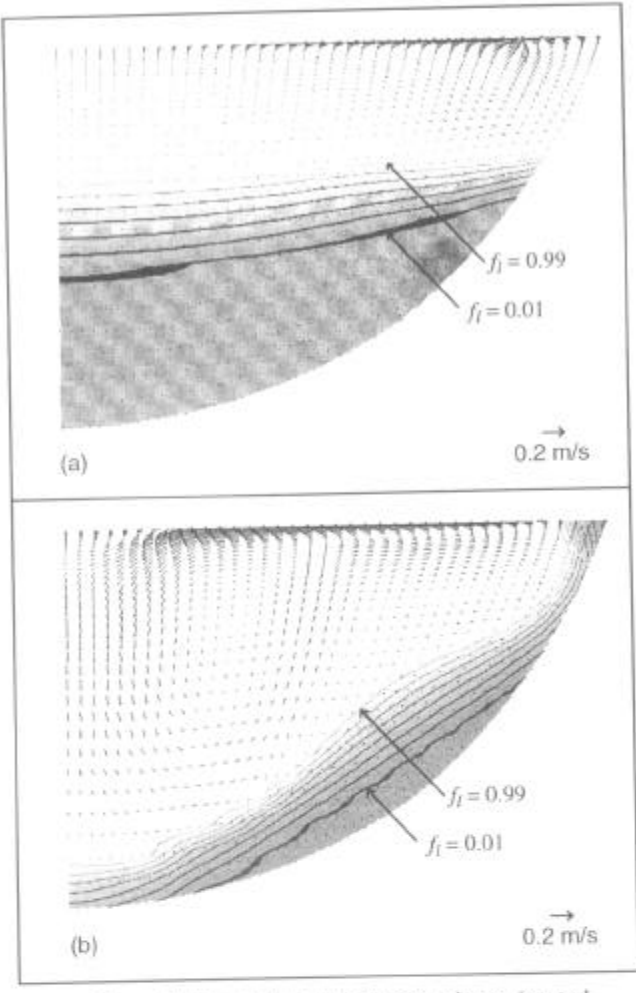


Figure 8. Predicted flow patterns using a 'central beam' with (a) a low sulphur content and (b) a high sulphur content.

Microstructural Predictions

The microstructural features of electron beam melted buttons were measured for buttons undergoing a controlled solidification stage iv processing. During this stage the electron beam moves inwards whilst the power is reduced. This process was modelled with r_b going from 35 mm to zero over 120 seconds whilst the power decays linearly from 2.6 kW to zero. The resulting predictions for λ_1 are shown in Figure 9(a) calculated using equation (11) with the material properties for Γ , D, m, C_m and k given in Table II. No predictions could be made in the bottom region of the button (cross-hatched area in Figure 9) because this area was already mushy in the steady state solution used as the initial condition for the model.

The values measured experimentally by Ellis⁸ are listed on the figure (in bold) beside the predicted values (in italics). Near the top of the button at the centre line the model prediction fails. This is the region to solidify last and the only area where the gradients are sufficiently low that a liquidus isotherm is predicted to enter from the top of the button due to radiative heat loss competing with conduction through the button. Experimentally this region is occasionally found to be equiaxed, indicating that the columnar dendrites can not grow in from the sides sufficiently quickly. The

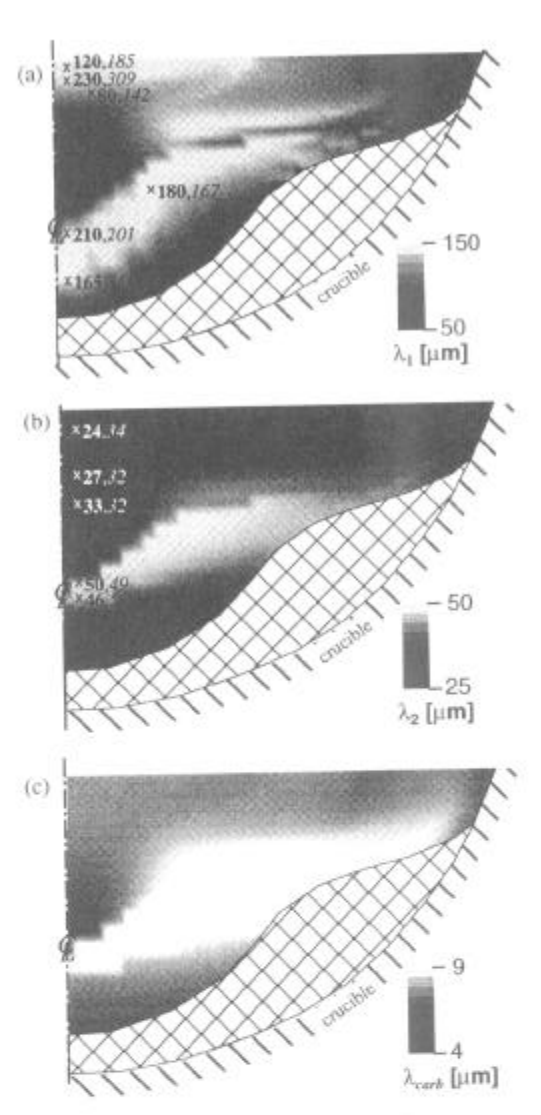


Figure 9. Predicted microstructural features for a button with a 120 s controlled solidification stage. (a) λ_1 , (b) λ_2 , and (c) λ_{cwb} . Experimentally measured values are in bold, predicted values are in italics.

 λ_1 model assumes that the growth is near steady state, and this assumption does not appear to hold in this region. When the columnar dendrites were found to extend to the top, the spacing was smaller than predicted, suggesting that the dendrites could not adjust their spacing in this relatively small distance. Pratt and Grugel^{11} have shown experimentally that the λ_1 adjust to order of magnitude changes in pull velocity during directional solidification experiments, suggesting either a slow response time to changes in thermal conditions or that the stable growth regime is large, adding a hysteresis effect.

The predictions for λ_2 are shown in Figure 9(b) calculated using equation (14). The correlation of predicted values to experimental is good. Predicted values for λ_{carb} are shown in Figure 9(c) calculated using equation (15). The carbide spacing was not measured experimentally.

Conclusions

Either the Lorentz or Marangoni force can be the governing factor for flow during secondary remelting processes, depending on the length scale and thermal gradients. The relative importance of these forces can be estimated by dimensionless analysis. A macromodel of the fluid flow and heat transfer was coupled to microstructural models to show that the changes in flow, caused by the different driving forces, have a large impact on the final microstructural features of the superalloy.

Many microstructural predictions can be made with straight forward correlation, for example λ_1 , λ_2 , and λ_{carb} . However, in the case of λ_1 a more complex model may be required to account for the response time and hysteresis of λ_1 to changes in thermal conditions.

The comparison of predicted to observed surface flows in electron beam melted buttons confirms that the Marangoni force is the main driving force for fluid flow in the EBBM process. Minor variations in the dependency of the surface tension on temperature can cause dramatically different flows, as shown by increasing the concentration of the surfactant sulphur from 6 to 20 ppm.

<u>Acknowledgements</u>

The authors would like to thank: Peter Quested, David Hayes and Ken Mills at the National Physical Laboratory for their assistance with both the experiments and the provision of material property data; the IRC in Materials for High Performance Applications, Birmingham, for providing experimental measurements of superalloy ingot to crucible heat fluxes; and Inco Alloys Ltd. for supplying both material and information. PDL would like to acknowledge the financial support of the EPSRC. RML would like to acknowledge the financial support of the DRA, Farnborough.

References

- 1. C. Hirsch, <u>Numerical Computation of Internal and External Flows</u>, Vol. 1 (John Wiley & Sons 1988).
- 2. M. McLean, <u>Directionally Solidified Materials for High Temperature Service</u>, (The Materials Society 1983), 28-33.
- 3. S.-Z. Lu, J.D. Hunt, "A Numerical Analysis of Dendritic and Cellular Array Growth: the Spacing Adjustment Mechanisms", J. Crystal Growth 123 (1992), 17-34.
- 4. J.D. Hunt and S.-Z. Lu, "Numerical Modelling of Cellular/Dendritic Array Growth: Spacing and Undercooling Predictions", <u>Modelling of Casting</u>, <u>Welding and Advanced Solidification Processes VII</u>, Ed. M. Cross and J. Campbell, (TMS 1995), 525-532.
- 5. A. Jardy, D. Ablitzer, J.F. Wadier, "Magnetohydrodynamic and thermal behavior of electroslag remelting slags." Met. Trans. 22B (1991), 111-120.
- 6. A. Jardy and D. Ablitzer, "On Convective and Turbulent Heat Transfer in VAR Ingot Pools", <u>Modelling of Casting, Welding and Advanced Solidification Processes V</u>, Ed. M. Rappaz *et al.*, (TMS 1990) 699-706.
- 7. P.N. Quested, D.M. Hayes, K.C. Mills, "Factors affecting raft formation in electron beam buttons", Mat. Sci. and Eng., A173 (1993), 371-377.
- 8. J. D. Ellis, "Quality Assurance by Electron Beam Button Melting", (Ph.D. thesis, Imperial College of Sci., Tech. and Med., 1992).

- 9. K.C. Mills, private communication with author, National Physical Laboratory, Teddington, 16 October, 1995.
- 10. M.J. McNallan and T. Debroy, "Effect of Temperature and Composition on Surface Tension in Fe-Ni-Cr Alloys Containing Sulfur", Met. Trans. 22B (1991), 557-560.
- 11. R.A. Pratt, R.N. Grugel, , "Microstructural Response to Controlled Accelerations During the Directional Solidification of Al-6 wt.% Si Alloys", Materials Charact. 31 (1993), 225-231.